Macromolecules

ARTICLE

pubs.acs.org/Macromolecules

Phase Diagrams of Electrostatically Self-Assembled Amphiplexes

Vesna Stanic,[†] Matthew Mancuso,[†] Waiken Wong,[‡] Elaine DiMasi,[§] and Helmut H. Strey[*,†]

[†]Department of Biomedical Engineering, Bioengineering Bldg, State University of New York at Stony Brook, Stony Brook, New York 11794-5281, United States

[‡]Polymer Science and Engineering Department, University of Massachusetts Amherst, Amherst, Massachusetts 10003, United States

[§]National Synchrotron Light Source, Brookhaven National Laboratory, Upton, New York 11973, United States

ABSTRACT: We present the phase diagrams of electrostatically self-assembled amphiplexes (ESA) comprised of poly(acrylic acid) (PAA), cetyltrimethylammonium chloride (CTACl), dodecane, pentanol, and water at three different NaCl salt concentrations: 100, 300, and 500 mM. This is the first report of phase diagrams for these quinary complexes. Adding a cosurfactant, we were able to swell the unit cell size of all long-range ordered phases (lamellar, hexagonal, *Pm*3*n*, *Ia*3*d*) by almost a factor of 2. The added advantage of tuning the unit cell size makes such complexes (especially the bicontinuous phases) attractive for applications in bioseparation, drug delivery, and possibly in oil recovery.

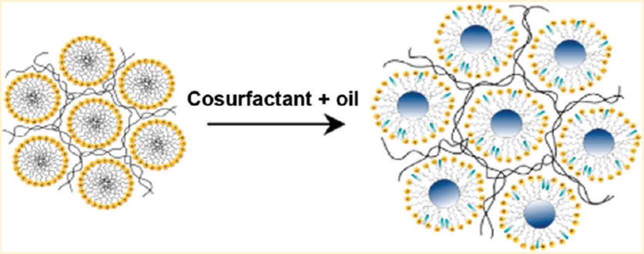

INTRODUCTION

The ease with which discrete and independent entities assemble into ordered objects and arrays in nature has been the underpinning of a great deal of scientific inquiry and application. Self-assembly occurs in a great variety of systems, ranging from nano- to microscale sized, organic to inorganic, biologically functioning to inert.[1] Subject merely to the fundamental forces that govern the behavior of its participating components—including electrostatics, hydrophobic/hydrophilic interactions, and hydrogen bonding—this process provides researchers routes to structures with low dispersity in terms of size, shape, and spacing. These mechanisms consequently are opening doors to current and potential advancements in fields as diverse as data storage, photonics, biomimetics, and catalysis.[2] Opportunities lie not only in using self-assembled materials as they occur naturally but also in manipulation of the system to suit the needs of the scientist, made possible through an understanding of the underlying physics.

One heavily used and studied self-assembling system is that of polyelectrolyte−surfactant complexes (PSCs).[3−10] Especially amenable to experimental study because of their aqueous nature, PSCs have provided insights into binding interactions between polymers and small molecules, solution properties of those same components, and morphological behavior of soft matter.[11−14] Moving from fundamental science and toward functional materials, PSCs show promise in uses including encapsulation of small molecules, separations, and templating for various types of nanostructures.[15−18]

The complex phase behavior of PSCs has been the subject of extensive study.[6,19−21] Various cubic symmetries, hexagonally packed cylinders, and lamellar stacks have all been observed and derive primarily from the action of the surfactant micelles and how they form long-rang ordered arrangements.[22] The PSC phase diagram has been studied as a function of polyelectrolyte charge density,[6,23,24] ionic strength and osmotic pressure.[5,6,25,26] The combination of solutions of surfactant micelles and polyelectrolyte at a condition of charge neutrality leads to precipitation of insoluble PSCs.

The mesophases available to PSCs are numerous as experimental parameters such as surfactant/polymer identity and ratio are changed. However, for a given pair at a ratio in the insoluble regime, there is far less flexibility to tune the morphology and unit cell size, primarily due to geometrical constraints imposed by the surfactant's molecular structure. The challenge becomes finding a method that allows, in a sense, to dial in a preferred morphology and unit cell size given the inherent spontaneous curvature and bending modulus of a particular species of surfactant micelle.

As one considers tuning the phase behavior and morphology of micelles, manipulating the spontaneous curvature and bending modulus becomes key (e.g., ref 27); reducing the modulus increases the flexibility of the surfactant layer, and it is only with greater flexibility and reduced spontaneous curvature that the micelles will be able to swell. Here we will reduce the spontaneous curvature of the surfactants using a cosurfactant as shown in Figure 1.

We will present a new type of self-assembled entity that bears some of the characteristics of micellar solutions and emulsions but also has properties unique from those systems: electrostatically self-assembled amphiphilic complexes, with further abbreviation of amphiphilic complex to amphiplex and the overall

Received: June 1, 2011
Revised: August 10, 2011
Published: August 25, 2011

dx.doi.org/10.1021/ma201240k | *Macromolecules* 2011, 44, 7423–7429

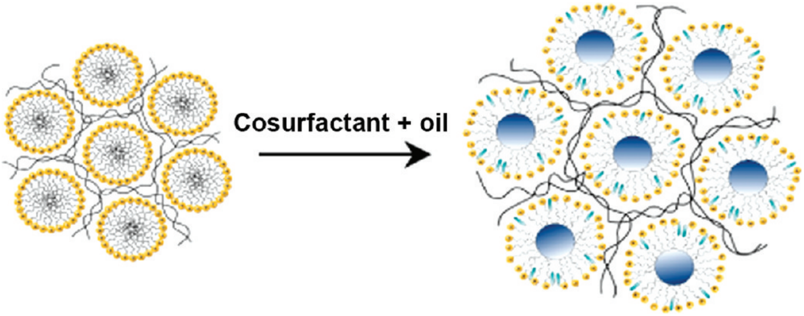

Figure 1. Schematic of a polyelectrolye−surfactant complex that is swollen with oil and cosurfactant.

acronym ESA. The term ESA captures all the important aspects of the materials to be described: the driving force for their creation, the demarcation between hydrophobic and hydrophilic domains stabilized by amphiphilic surfactant molecules, and the fact that these are long-range ordered materials.

■ EXPERIMENTAL SECTION

Materials. Poly(acrylic acid) (PAA) sodium salt with M_w = 5100 g/mol, cetyltrimethylammonium chloride 25% solution in water (CTACl), dodecane (99+%), 1-pentanol (99+% extra pure) were obtained from Sigma-Aldrich. Millipore water was used to make PAA solutions while other chemical are used as purchased. Maintaining polyelectrolyte/surfactant stoichiometry charge ratio 1:1, we explore series of samples at three different NaCl salt concentrations of 100, 300, and 500 mM. All samples were prepared in commercial 96-well plates. In order to obtain the desiderate salt concentration, appropriate amounts of PAA and CTACl solutions were added to each well. For each salt concentration we prepared samples containing all combinations of 0, 2, 6, 10, 20, 30, 40, 50, and 60% pentanol ($w_{\text{pentanol}}/w_{\text{CTACl}}$) and 0, 20, 40, 60, 80, 100, 120, 140, 160, 180, 200, and 220% dodecane ($w_{\text{dodecane}}/w_{\text{CTACl}}$). Equilibration and X-ray measurements were performed at room temperature (25 °C).

SAXS Measurements and Data Analysis. Synchrotron small-angle X-ray scattering (SAXS) experiments were performed at the National Synchrotron Light Source Beamline X6B at Brookhaven National Laboratories (BNL) at the incident wavelength of 1.24 Å (10 keV). We used a two-dimensional detector located about 100 cm from the sample allowing us to investigate the q range from 0.02 to 0.39 Å^{-1} (q is the scattering vector, $q = 4\pi \sin \theta/\lambda$, where λ is the X-ray wavelength and 2θ is the scattering angle). The q-range calibration was performed with a silver behenate standard. The X-ray diffraction was performed automatically using a combinatorial sample scanner capable of measuring hundreds of samples per hour. All samples were equilibrated for at least 1 week before measurements.

Phase identification was performed by fitting all observable peaks to Lorenzian's using the MultiPeak Fitting routine provided by Igor Pro 6.1. The minimum requirements for identification of a phase or mixture of phases were the observation of the most intense and significant peaks for each phase, i.e., at least 2 peaks for lamellar, (1 and 2), 3 peaks for hexagonal ($1, \sqrt{3}, 2$), 4 peaks for $Pm3n$ ($\sqrt{2}, \sqrt{4}, \sqrt{5}, \sqrt{6}$), and 4 peaks for $Ia3d$ ($\sqrt{6}, \sqrt{8}, \sqrt{22}, \sqrt{24}$).

Combinatorial X-ray Scattering Setup. For this study we designed combinatorial material science X-ray diffraction instrumentation to measure the nanoscale structure of our self-assembled soft materials as a function of composition. Our design is especially useful but not limited to the field of soft matter where samples are often liquid and/or liquid crystalline.

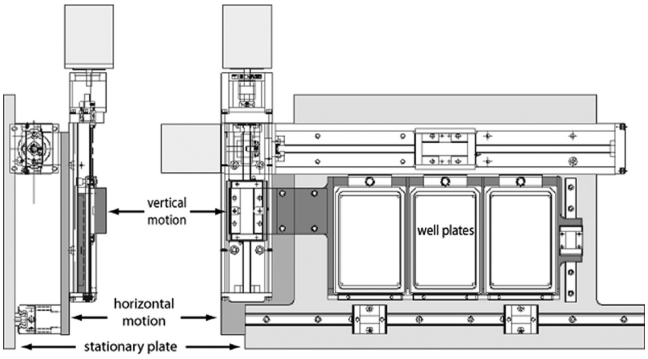

Figure 2. Schematics of the well plate scanner. Depictions of the structural plates on the front view (right) are schematically shown "behind" the carriage rails, drive screws, and motor mounting hardware so that additional details may be seen. The side view (left) is an accurate assembly profile.

We chose to design our sample platform around standard well plates (American National Standards Institute in conjunction with the Society for Biomolecular Sciences ANSI/SBS 1-2004 through ANSI/SBS 4-2004) that provides specificiations for footprint, height, and bottom outside flange dimensions as well as standardized well positions. The advantage of using a widely accepted standard sample platform is that there exists a tremendous number of different well plates (varying in material, well shape, and depth) and equipment that fit the standard footprint such as shakers, robotic systems, centrifuge rotors, multipipetters, and sealers. Throughout our studies we used 96-well poly(styrene) plates (Greiner BioOne) because their wells are open on both ends and can be sealed easily by thin Mylar or Kapton films that exhibit low X-ray absorbance.

Central to the instrumentation is a motorized stage that can hold up to three well-plates at a time and is capable of positioning the X-ray beam quickly and reproducibly to any of the individual samples contained in these plates. Faster sample changing and alignment rates allow the collection of X-ray diffraction data at unprecedented speeds. Additionally, the setup is fully integrated into the beamline's control software allowing it to be operated in an automated and computer-controlled fashion.

We designed our $x-y$ translational stage to fit into the existing X6B beamline architecture. This translational stage, called the well plate scanner, mounts onto the Eulerian cradle of the X6B goniometer (Huber 512) already present at the beamline. This compatibility allows the beamline to be rapidly reconfigured between users and makes it possible to rock crystalline samples.

A plate supporting horizontal motion is mounted on carriage rails on the stationary plate and carries a vertical drive that moves the well plate mounting assembly. The motors driving the lead screws are IMS (Intelligent Motion Systems, Inc.) MDrive stepping motors with integrated microstepping drivers. Motion is reproducible without backlash correction.

Schematics used to create the well plate scanner appear in Figure 2, and an illustration of its position in the beamline is shown in Figure 3.

Motor control is fully integrated into SPEC (Certified Scientific Software) along with the other beamline systems (CCD, shutters, Huber goniometer movements) creating a fully integrated environment. Macros are written for simple functions including moving to specific wells, specific plates, and predetermined loading positions as well as more complex linear and two-dimensional scans of collections of wells and entire plates. These macros can be configured to scan different size well plates, to set exposure times, etc. For more complex systems it is possible to define custom macros changing combinations of these variables dynamically during data collection.

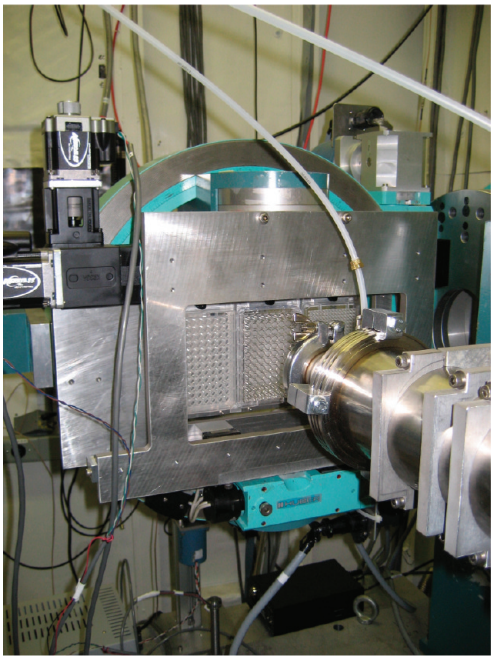

Figure 3. The well plate scanner is shown mounted at the beamline. Beam is incident on the well plates from behind, and the transmitted and scattered intensities enter the vacuum flight path in the foreground of the photo, to be measured by a photodiode beam stop and an area detector, respectively.

Automation of the well plate scanning system allows us to measure more than a thousand individual samples per day. To take full advantage of this system, it is necessary to prepare large quantities of samples in an efficient manner. In order to reduce preparation time and make sample preparation simpler, we developed scripts in Python that will be made available on the NSLS X6B Web site. With these scripts it is possible to calculate and change composition and concentration of each well quickly and accurately. The software produces not only spreadsheets that are used for filling well plates but also Extensible Markup Language (.xml) files which can later be used to link the sample composition to the X-ray scattering results in an automated fashion.

For our work, the well plate scanning system improved our throughput by a factor of 6−7 depending on exposure time. Even though the improvement in throughput seems significant we anticipate even larger gains when adopting our technology to third generation sources such as NSLS-II. Anticipating that a 50−1000 times higher flux is achievable at a third generation synchrotron source and faster readout detectors (current pixel array detector technology can achieve readout rates of 300 Hz, e.g. Pilatus 100k, Detris, Switzerland), we can push the sample throughput to significantly less than 1 s per sample. At this point it may become necessary to introduce a robotic sample changer to achieve a fully automated beamline. Such mode of operation is ideally suited for "rapid access" users and will enable use of high-resolution (significantly better than laboratory-based X-ray sources) X-ray scattering experiments that are much better suited to basic material science research than access by cycle (typically three times a year). In a "rapid access" mode a user could send in (possibly by mail) well plates containing several hundred samples once a week and receive the scattering data within 24 h. This would allow a much more effective feedback for optimizing material design and is much more compatible with the academic workflow.

We hope that our combinatorial setup will benefit and improve our understanding of the phase behavior of multicomponent system that in turn will allow the design of novel materials for applications in medicine, personal care, pharmacology, energy conversion, agriculture, and petroleum.

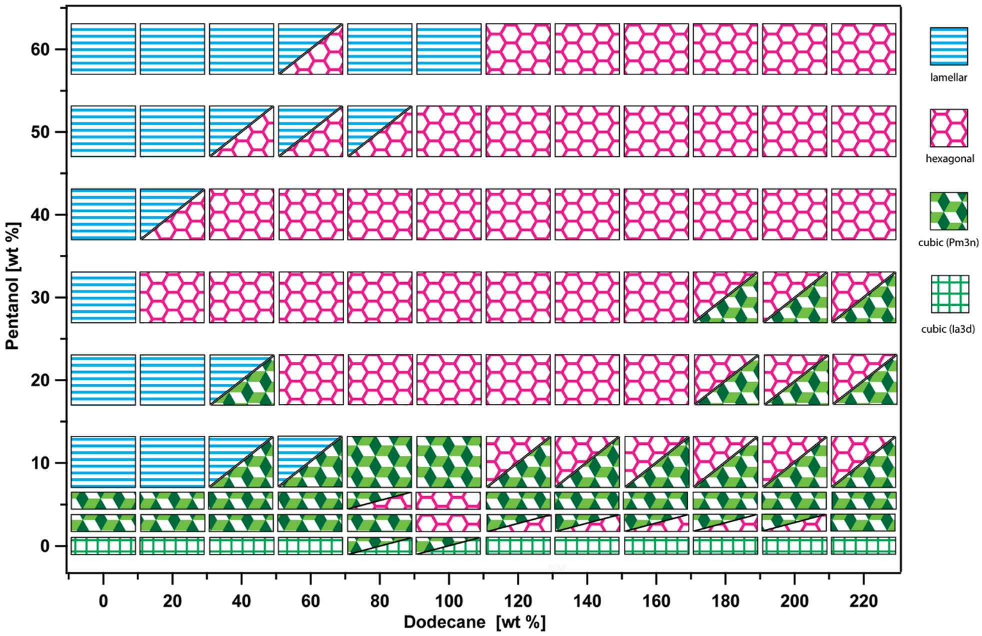

Figure 4. Phase diagram of ESA complexes at 100 mM NaCl salt concentration as a function of pentanol and dodecane content relative to the surfactant weight [wt %].

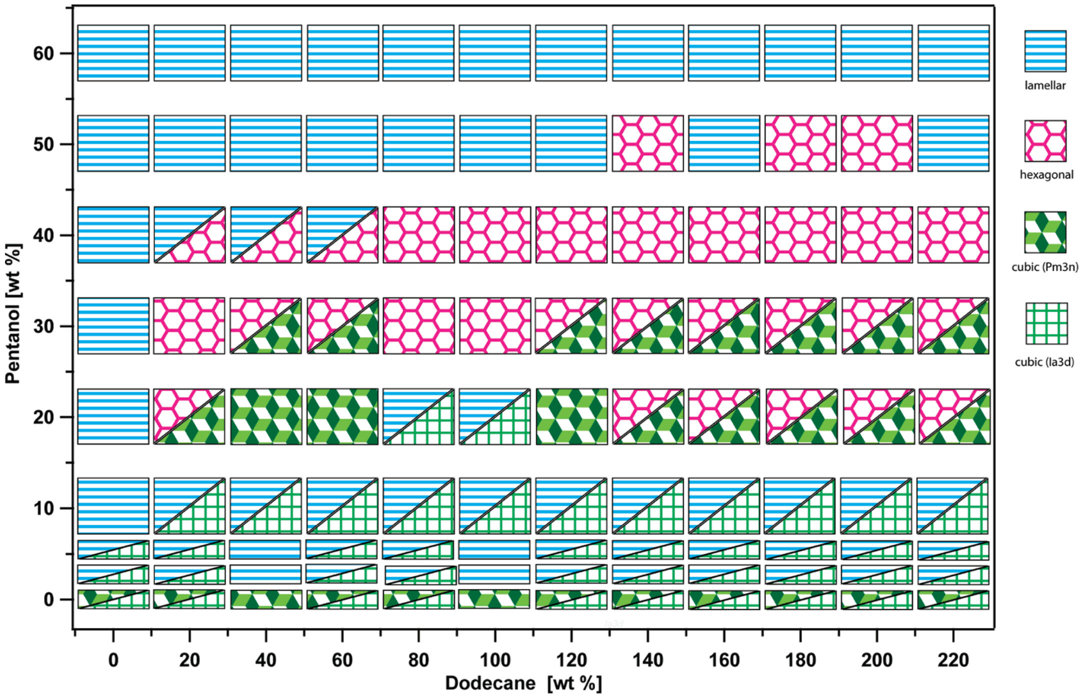

Figure 5. Phase diagram of ESA complexes at 300 mM NaCl salt concentration as a function of pentanol and dodecane content relative to the surfactant weight [wt %].

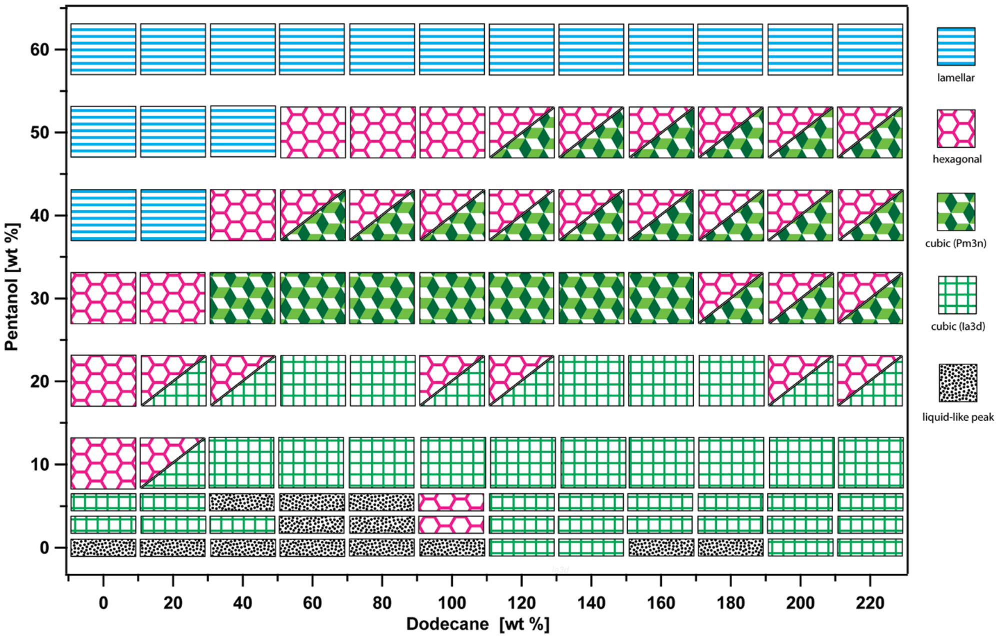

Figure 6. Phase diagram of ESA complexes at 500 mM NaCl salt concentration as a function of pentanol and dodecane content relative to the surfactant weight [wt %].

■ RESULTS AND DISCUSSION

Phase Diagrams. Traditional phase diagrams of multicomponent systems are studied over the whole composition space. However, our system precipitates out of solution, and therefore a full range of compositions is not available. Furthermore, as will become clear later in the discussion of our results, not all added oil (dodecane) is incorporated into the structures leading to further phase separation. Similarly, adding too much cosurfactant will lead to disordered liquidlike structures. For this reason, we chose to study only a limited range of cosurfactant and oil concentrations for which long-range ordered can be observed. To understand the phase organization and nature of phase transition, we performed systematic synchrotron X-ray measurements on electrostatically self-assembled amphiplexes with compositions described in the Experimental Section at three different

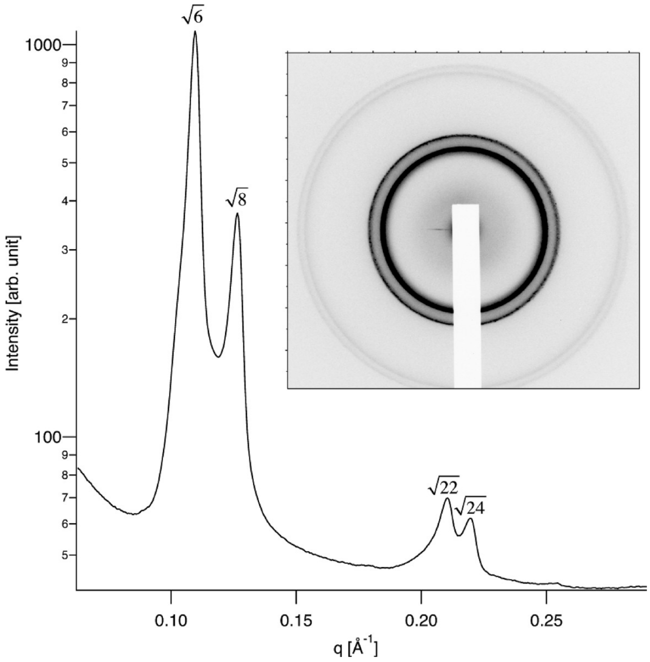

Figure 7. SAXS pattern of cubic *Ia*3*d* phase at 100 mM NaCl salt for the PAA–CTACl complex.

NaCl salt concentrations. The phase behavior as a function of oil and cosurfactant concentration at fixed surfactant-to-polyelectrolyte ratio (1:1) is shown in Figures 4, 5, and 6 for 100, 300, and 500 mM NaCl salt, respectively.

At 100 mM NaCl salt solution in the absence of oil and cosurfactant the PAA–CTACl complex yields a white precipitate that exhibits a cubic *Ia*3*d* structure as shown in Figure 7. It should be noted that reflections $\sqrt{14}$ and $\sqrt{16}$, which are usually present in this phase, are missing here. Nevertheless, the intensity ratio between the first and second peaks is consistent with the bicontinuous *Ia*3*d* morphology (we measure a ratio of 6:1 for $I_{\sqrt{6}}$:$I_{\sqrt{8}}$), originally identified by Luzzati and Spegt,[28] and commonly observed in lipid and other surfactant systems.[29] By adding a small amount of cosurfactant (2 wt %) to the PAA–CTACl system, we find *Pm*3*n* phases at all oil concentrations. This phase, which is also known as the A15 lattice and the β tungsten lattice, has been observed frequently in similar hard core/soft corona colloidal systems.[24,30,31] It is now commonly believed that the *Pm*3*n* structure is formed by disconnected micellar aggregates.[32] Its existence has been addressed theoretically by Kamien and co-workers,[33] who used a modified hard-core/soft-shell potential to model its evolution from close-packed cubic structures. The *Pm*3*n* phase is believed to arise from frustration between the hard-core excluded-volume interaction and the surface interaction due to overlapping soft coronas and, as such, illustrates the so-called "close packing vs minimal area" principle. In our case, polyelectrolyte chains surrounding the oil-filled surfactant micelles comprise the soft shell. A transition into the lamellar phase occurs after the amount of cosurfactant exceeds 6 wt % with maximum incorporation of 120 wt % of oil with respect to the surfactant. However, above 20 wt % of oil and 20 wt % of cosurfactant the hexagonal phase undergoes a transition leading to a single-phase region of the hexagonal phase. In general, the 100 mM phase diagram is dominated by the hexagonal phase with relatively small coexisting phase regions as compared to 300 and 500 mM NaCl phase diagrams. All phase diagrams show stable hexagonal and lamellar phases at high cosurfactant content and low oil concentration.

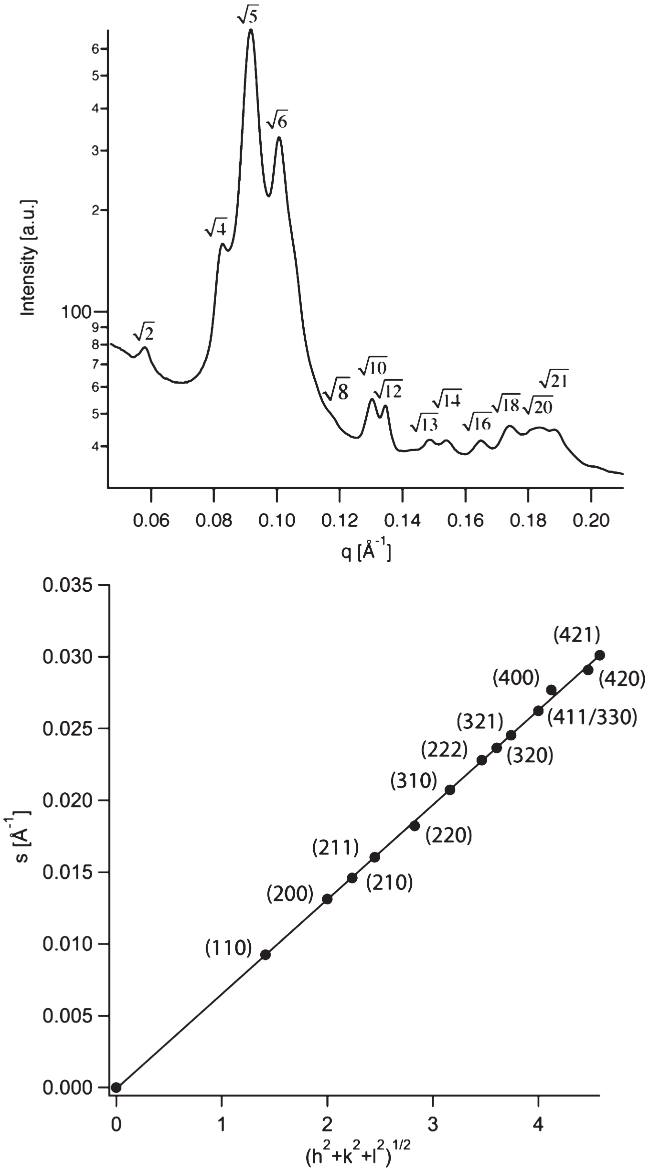

Figure 8. Small-angle X-ray diffraction spectrum of the ESA complex at 80 wt % of dodecane and 10 wt % of pentanol with respect to the surfactant (100 mM NaCl salt). A total of 11 Bragg peaks of the cubic *Pm*3*n* phase are observed. The ratio of the reciprocal spacing with corresponding plot of s ($s = 1/d_{hkl}$) vs $(h^2 + k^2 + l^2)^{1/2}$ is given.

At 300 mM and especially 500 mM, at low concentration of cosurfactant (up to 10 wt %) we find regions with liquidlike order characterized by a single diffuse X-ray scattering peak. As shown in Figures 5 and 6, cubic structures *Pm*3*n* and *Ia*3*d* cover a large area in both phase diagrams, reducing the amount of lamellar and hexagonal phases.

Swelling Effect. In our experiments, we found that the swelling of the unit cell size a in each phase depends on two parameters: (1) the concentration of the cosurfactant that acts on the spontaneous curvature of surfactant and (2) the amount of oil that incorporates into the lipophilic part of the surfactant. The unit cell size a is calculated using the following equations: for the

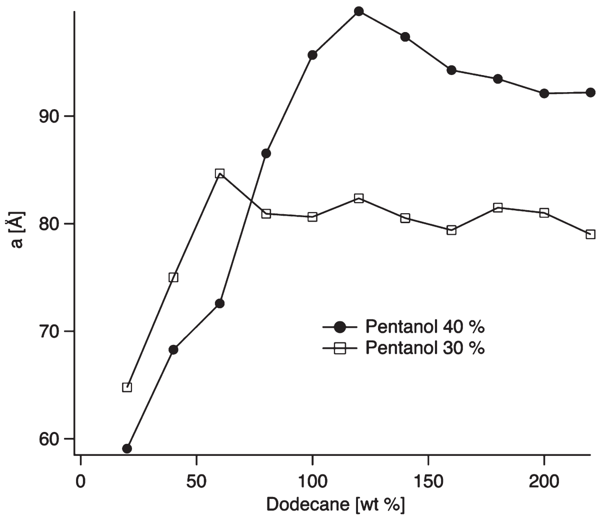

Figure 9. Swelling of hexagonal phase as a function of pentanol increase at 100 mM NaCl salt concentration.

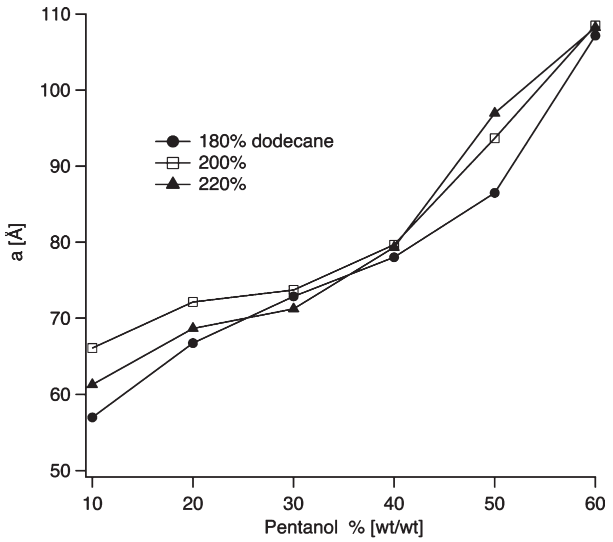

Figure 10. Unit cell parameter *a* versus dodecane content for hexagonal phase at 300 mM NaCl salt concentration for 30% and 40% of pentanol.

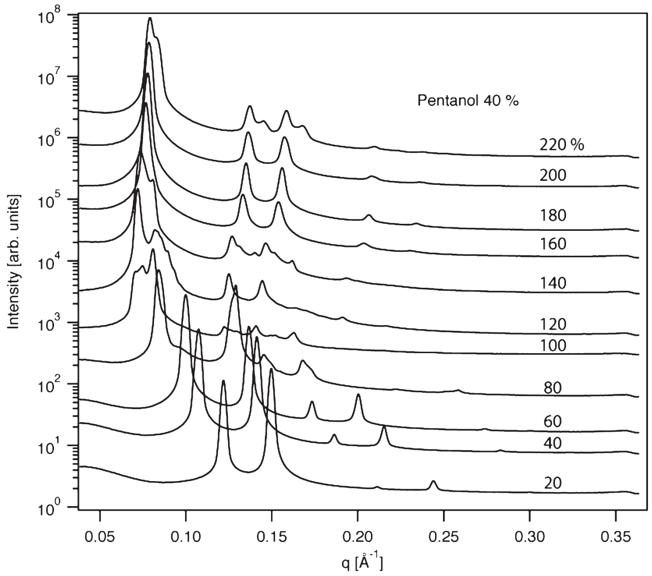

Figure 11. SAXS patterns of the hexagonal phases as a function of dodecane increase at pentanol concentration of 40% for the 300 mM NaCl salt concentration. At 80−140% and at 220% dodecane the samples had partially dried which explains the peak splitting. The samples remained purely hexagonal, however.

hexagonal (hcpc) phase $1/d_{hkl} = 2(h^2 + k^2 + hk)^{1/2}/\sqrt{3}a$ and for the cubic phases $1/d_{hkl} = (h^2 + k^2 + l^2)^{1/2}/a$. To determine the space group of the of the cubic phases (*Pm*3*n* or *Ia*3*d*), we plot = $(h^2 + k^2 + l^2)^{1/2}$ versus the reciprocal *d*-spacings ($s = 1/d_{hkl}$). An example of the SAXS intensity profile with Miller indexes (*hkl*) is shown in Figure 8. For a cubic phase, such a plot should pass through the origin and be linear with slope of *a*. As shown in Figure 8, we observe 13 spacings with ratios of $\sqrt{2}$, $\sqrt{4}$, $\sqrt{5}$, $\sqrt{6}$, $\sqrt{8}$, $\sqrt{10}$, $\sqrt{12}$, $\sqrt{13}$, $\sqrt{14}$, $\sqrt{16}$, $\sqrt{18}$, $\sqrt{20}$, and $\sqrt{21}$, which are typical for the *Pm*3*n* phase. Figure 9 shows the swelling of the unit cell parameter *a* of hexagonal phases (from 57.0 to 108.2 Å) as a function of cosurfactant addition for 100 mM NaCl salt concentration. From Figure 9 it is evident that at high oil concentration the unit cell size does not grow when more oil is added. An example of swelling of the unit cell parameter *a* of the hexagonal phase as a function of oil concentration is reported in Figure 10 at 300 mM salt. The unit cell parameter *a* increases linearly with oil concentration up to 60% (w/w) oil at 30% (w/w) cosurfactant and up to 120% (w/w) oil at 40% (w/w) of cosurfactant. Above those maximum oil concentrations the swelling curve reaches a plateau, indicating the limit of oil incorporation at a specific cosurfactant concentration. Further, these results are supported also by trends of SAXS patterns shown in Figure 11. We found similar behaviors throughout the three phase diagrams when tracking the unit cell as a function of oil content in a single-phase region (for lamellar, hexagonal, and cubic phases).

Our results are consistent with previous work on quaternary systems of cetyltrimethylammonium bromide/water/*n*-pentanol/*n*-hexane[34,35] and sodium dodecyl sulfate/water/pentanol/dodecane.[36,37] In these systems an increase in interfacial pentanol lead to a decrease in spontaneous curvature. (In this case we define positive curvature relative to the head-to-tail orientation which means that additional pentanol will induce a transition from micelles (positive curvature) to inverse micelles (negative curvature).) For example, Palazzo[35] found that an increase in interfacial pentanol lead to a decrease in inverted micelle radius. This study also established that the molar ratio of interfacial pentanol is controlled by the surfactant/cosurfactant and cosurfactant/oil ratio. The water content contributes to a lesser extent since the cosurfactant solubility in water is negligible compared to the solubility in oil (e.g., solubility of 1-pentanol in oil is 2.7%). Generally, the solubility of cosurfactants is greatest in the surfactant layer, moderately high in the oil, and negligible in the water phase. The consequences of these facts are as follows. Increasing oil content while keeping the cosurfactant content constant leads to a decrease in cosurfactant concentration in the surfactant layer and leads to an increase in spontaneous curvature (e.g., lamellar → hexagonal → cubic). In order to maintain a constant cosurfactant concentration in the interface, one has to move in a diagonal in the phase diagrams (Figures 4−6). This explains why most phase boundaries are found along diagonals.

Table 1. Minimum and Maximum Values (in Å) of Unit Cell Parameter *a* for Each Phase Observed at Three Different Salt Concentrations

	lamellar	hexagonal	cubic *Pm*3*n*	cubic *Ia*3*d*
100 mM NaCl	42.3−54.5	57.0−108.2	119.6−164.1	130.7−145.9
300 mM NaCl	44.1−80.0	59.1−125.2	111.9−236.9	135.8−180.0
500 mM NaCl	41.6−77.2	54.7−106.2	208.0−268.6	164.0−180.7

This also explains why the oil swelling curves saturate (Figures 9 and 10). In order to incorporate oil into micellar structures, the spontaneous curvature has to be reduced using cosurfactant. As the micelles swell, the incorporated oil dissolves more and more cosurfactants effectively depleting the interface layer and as a consequence the micelles stop growing.

Finally, Table 1 summarizes the minimum and maximum swelling of unit cell parameter *a* for all observed phases at three different salt concentration. Swelling of the unit cell is clearly affected by salt concentration. Most notable is the doubling in unit cell size for cubic *Pm*3*n* phases as the salt concentration is increased. On the other hand, for lamellar and hexangonal phases increasing the salt concentration from 300 to 500 mM seems to decrease the unit cell size range. Similar findings were reported for some quaternary systems[38] where the authors observed that higher salt concentration reduced lamellar swelling. In our case it is more likely that these ranges are reduced because of the competition and phase coexistence with the cubic phases.

■ CONCLUSION

In summary, we reported the phase diagrams of quinary electrostatically self-assembled amphiplexes (ESA). We were able to incorporate large amounts of oil into long-range ordered ESA structures and consequently almost doubling the unit cell size of all phases. The added advantage of tuning the unit cell size makes such complexes (especially the bicontinuous phases) attractive for applications in bioseparation, drug delivery, and possibly in oil recovery.

■ AUTHOR INFORMATION

Corresponding Author

*E-mail: Helmut.Strey@stonybrook.edu.

■ ACKNOWLEDGMENT

This project was supported by the Office of Basic Energy Sciences, Materials Sciences and Engineering Division, of the U.S. Department of Energy under Grant ER46323. The National Synchrotron Light Source is supported under U.S. DOE Contract No. DE-AC02-CH10886. We also acknowledge support for W. Wong from the National Science Foundation through the University of Massachusetts Amherst Materials Research Science and Engineering Center (DMR-0213695).

■ REFERENCES

(1) Whitesides, G. M. *Proc. Natl. Acad. Sci. U. S. A.* **2002**, *99* (8), 4769–4774.

(2) Ariga, K.; Hill, J. P.; Lee, M. V.; Vinu, A.; Charvet, R.; Acharya, S. *Sci. Technol. Adv. Mater.* **2008**, *9* (1), 014109.

(3) Antonietti, M.; Burger, C.; Effing, J. *Adv. Mater.* **1995**, *7* (8), 751–753.

(4) Berret, J. F.; Oberdisse, J. *Physica B: Condens. Matter* **2004**, *350* (1−3), 204–206.

(5) Ilekti, P.; Piculell, L.; Tournilhac, F.; Cabane, B. *J. Phys. Chem. B* **1998**, *102* (2), 344–351.

(6) Leonard, M. J.; Strey, H. H. *Macromolecules* **2003**, *36* (25), 9549–9558.

(7) Leonard, M.; Strey, H. H. *Macromolecules* **2010**, *43* (9), 4379–4383.

(8) Zhou, S.; Hu, H.; Burger, C.; Chu, B. *Macromolecules* **2001**, *34*, 1772–1778.

(9) Nause, R. G.; Hoagland, D. A.; Strey, H. H. *Macromolecules* **2008**, *41* (11), 4012–4019.

(10) Piculell, L.; Norrman, J.; Svensson, A. V.; Lynch, I.; Bernardes, J. S.; Loh, W. *Adv. Colloid Interface Sci.* **2009**, *147−48*, 228–236.

(11) Faul, C. F. J.; Antonietti, M. *Adv. Mater.* **2003**, *15* (9), 673–683.

(12) Goddard, E. D. *Colloids Surf.* **1986**, *19*, 301–329.

(13) Ober, C. K.; Wegner, G. *Adv. Mater.* **1997**, *9* (1), 17–31.

(14) Stanley, C. B.; Strey, H. H. *Soft Matter* **2008**, *4* (2), 241–244.

(15) Bronich, T. K.; Nehls, A.; Eisenberg, A.; Kabanov, V. A.; Kabanov, A. V. *Colloids Surf., B* **1999**, *16* (1−4), 243–251.

(16) Schwarz, H.; Apostel, R.; Paul, D. *J. Membr. Sci.* **2001**, *194* (1), 91–102.

(17) Tao, C.; Li, J. *Langmuir* **2003**, *19* (24), 10353–10356.

(18) Bernardes, J. S.; Norrman, J.; Piculell, L.; Loh, W. *J. Phys. Chem. B* **2006**, *110* (46), 23433–42.

(19) Antonietti, M.; Conrad, J.; Thünemann, A. *Macromolecules* **1994**, *27*, 6007–6011.

(20) Antonietti, M.; Burger, C.; Conrad, J.; Kaul, A. *Macromol. Symp.* **1996**, *106*, 1–8.

(21) Thalberg, K.; Lindman, B.; Bergfeldt, K. *Langmuir* **1991**, *7*, 2893–2898.

(22) Seddon, J. M. *Biochim. Biophys. Acta* **1990**, *1031*, 1–69.

(23) Kogej, K.; Theunissen, E.; Reynaers, H. *Langmuir* **2002**, *18*, 8799–8805.

(24) Zhou, S.; Burger, C.; Yeh, F.; Chu, B. *Macromolecules* **1998**, *31*, 8157–8163.

(25) Mya, K.; Sirivat, A.; Jamieson, A. M. *J. Phys. Chem. B* **2003**, *107* (23), 5460–5466.

(26) Thalberg, K.; Lindman, B.; Karlstrom, G. *Prog. Colloid Polym. Sci.* **1991**, *84*, 8–12.

(27) Koltover, I.; Salditt, T.; Radler, J. O.; Safinya, C. R. *Science* **1998**, *281* (5373), 78–81.

(28) Luzzati, V.; Spegt, P. A. *Nature* **1967**, *215* (5102), 701.

(29) Forster, S.; Khandpur, A. K.; Zhao, J.; Bates, F. S.; Hamley, I. W.; Ryan, A. J.; Bras, W. *Macromolecules* **1994**, *27* (23), 6922–6935.

(30) Fontell, K. *Colloid Polym. Sci.* **1990**, *268*, 264–285.

(31) Ilekti, P.; Martin, T.; Cabane, B.; Piculell, L. *J. Phys. Chem. B* **1999**, *103*, 9831–9840.

(32) Seddon, J. M.; Templer, R. H. *Philos. Trans. R. Soc. London, Ser. A: Math. Phys. Eng. Sci.* **1993**, *344* (1672), 377–401.

(33) Ziherl, P.; Kamien, R. D. *Phys. Rev. Lett.* **2000**, *85* (16), 3528–3531.

(34) Palazzo, G.; Carbone, L.; Colafemmina, G.; Angelico, R.; Ceglie, A.; Giustini, M. *Phys. Chem. Chem. Phys.* **2004**, *6* (7), 1423–1429.

(35) Palazzo, G.; Lopez, F.; Giustini, M.; Colafemmina, G.; Ceglie, A. *J. Phys. Chem. B* **2003**, *107* (8), 1924–1931.

(36) Bellocq, A. M.; Roux, D. In *Microemulsions, Structure and Dynamics*; Friberg, S., Bothorel, P., Eds.; CRC Press: Boca Raton, FL, 1987; p 33.

(37) Freyssingeas, E.; Roux, D.; Nallet, F. *J. Phys.: Condens. Matter* **1996**, *8* (16), 2801–2806.

(38) Maugey, M.; Bellocq, A. M. *Langmuir* **1999**, *15* (25), 8602–8608.